Dry hyperbaric welding of HSLA steel up to 35 bar ambient pressure with CMT arc mode

Ivan Bunaziv[*], Ragnhild Aune, Vigdis Olden, Odd M. Akselsen

SINTEF Industry, P.O. Box 4760 Torgarden, NO-7465 Trondheim, Norway

* Corresponding Author's Email: ivan.bunaziv@sintef.no

Abstract

Hyperbaric welding plays a significant role in subsea pipeline installations and repairs for transport of oil and gas from the offshore field to the market. The effect of ambient pressure, from 1 to 35 bar, on penetration depth and microstructure evolution in dry hyperbaric welding of X70 pipeline steel has been investigated. It was found that penetration depth is increasing with increased ambient pressure due to enhanced melt flow by using the cold metal transfer (CMT) arc mode. Increase ambient pressure lowered process stability causing more spattering strongly affecting current/voltage characteristics of the arc. Numerical simulation showed very fast cooling rate regardless ambient pressure effect causing hard microstructure. Application of lower alloyed wire provided lower hardenability and higher fraction of the allotriomorphic ferrite with high acicular ferrite volume fraction. Chemical analysis revealed positive effect of low oxygen/nickel with high silicon containing wire for acicular ferrite nucleation in weld metal at any process parameters due to higher activity of inclusions.

Keywords: Dry hyperbaric welding; Cold metal transfer; Numerical simulation; Microstructure; HSLA steel; Non-metallic inclusions

Nomenclature	
C_p	specific heat (J kg^{-1} °C^{-1})
F_{EM}	electromagnetic force (N m^{-3})
f	mass proportion of molten material
g	standard acceleration due to gravity (9.8 m s^{-2})
H	enthalpy (kg m^2 s^{-2})
H_L	latent heat of fusion (230000 J kg^{-1} °C^{-1})
h_c	heat transfer coefficient for convection (50 W m^{-2} °C^{-1})
I	arc current (A)
k	thermal conductivity (W m^{-1} °C^{-1})
L_B	characteristic length which is approximated by 1/8 of weld pool width (m)
L_P	length of weld pool (m)
n	outward normal vector of top surface
P	power of the Gaussian surface heat source (W)
P_A	arc pressure (N m^{-2})
Q_{in}	heat input of the volumetric heat source model (kJ/mm)

Q_t	total heat flux of the heat source (W m^{-3})
r	radius of the Gaussian surface heat source (m)
R_1	radius of arc at welding electrode (m)
R_2	radius of arc at weld pool surface (m)
T_0	ambient temperature (20 °C)
T_L	liquidus temperature (1512 °C)
T_S	solidus temperature (1472 °C)
U	arc voltage (V)
v_d	momentum diffusitivity or kinematic viscosity (m^2 s^{-1})
v_{max}	characteristic (or maximum) melt velocity in weld pool (m s^{-1})
v_t	volumetric heat source travel speed (mm/min)
Greek symbols	
α	thermal diffisitivity (m^2 s^{-1})
β	thermal expansion coefficient (1.0 × 10^{-5} m m^{-1} °C^{-1})
ΔT	temperature difference of maximum temperature in weld pool and solidus temperature (°C)
$d\gamma/dT$	thermal gradient of surface tension (−0.35 × 10^{-4} N m^{-1} °C^{-1})
ε	emissivity rate (0.5)
η	arc efficiency (0.8 for GMAW process)
μ_0	permeability in a vacuum (1.257 × 10^{-6} N A^{-2})
μ_d	dynamic viscosity of the liquid metal (N s m^{-2})
μ_L	viscosity of the liquid metal (3 × 10^{-2} kg m^{-1} s^{-1})
μ_m	magnetic permeability (1.26 × 10^{-6} N A^{-2})
ρ_L	density of the liquid metal (6800 kg m^{-3})
ρ_S	density of the solid metal (7800 kg m^{-3})
σ	Stefan-Boltzmann constant (5.67 × 10^{-8} W m^{-2} °C^{-4})

1. Introduction

In the offshore industry, hyperbaric welding of pipelines is commonly used method for subsea operations in order to expand the pipeline network for transport of oil and gas from the field to the market. In addition, welding is used for repair, and the authorities require often that operating company have emergency welding procedures in case of leakage or damage to the pipe. Nowadays, the maximum depth of diver assisted operation is limited to 180 meters in order to avoid health or safety risks for the divers based on Richardson et al. [1]. Fully remote-controlled and robust welding systems are therefore needed for such applications since oil and gas can be found at very deep waters, beyond 2000 meter depth according to Hart [2]. Furthermore, an extension of existing pipeline networks by using hot-tapping technology also requires remote controlled welding processes.

Welding at higher ambient pressure is different compared to atmospheric. Under higher ambient pressure the arc is constricted, reduced arc root size, and the arc width can be smaller than the diameter of the electrode according to Akselsen et al. [3]. Therefore, the arc carries more energy since the current density is higher. According to Azar [4], the ionization temperature of the shielding gas is increasing, thus, more energy is required to sustain appropriate the arc shape. Therefore, the arc shape volume is suppressed. The arc has a *wandering* behavior, employing unstable processing based

on Richardson and Nixon [5]. Ofem et al. [6] stated that smaller dimensions of weld pool, due to constricted arc and enhanced heat extraction due to ambient conditions, provides increased cooling rate at higher ambient pressures. It was confirmed by Azar et al. [7] that at higher pressures the cooling rate of weld metal is increasing. This may cause solidification cracking and development of unfavorable microstructures such as martensite or bainite. According to Nixon [8] the chemistry of the weld pool and arc structure is changed. Higher water vapor content in dry hyperbaric welding results in chemical reactions and gas absorption at the weld pool surface according to Richardson et al. [1]. Repelled metal transfer and spattering also occur due to the difference in current density between the arc column and the arc root forming of opposing electromagnetically driven plasma jets according to Richardson and Nixon [9]. Up to recently, dry hyperbaric welding was employed with conventional gas metal arc welding (GMAW) using pulsed arc mode. The relatively new cold metal transfer (CMT) has not yet been studied widely under hyperbaric welding conditions. It is expected that CMT would be suitable for deposition of root pass, which is a critical part in hyperbaric welding for oil and gas industry. CMT is a dip-transfer mode with reciprocating filler wire motions allowing more controllable process based on Schörghuber [10]. Here, the filler wire is transferred by short-circuiting phase with no free-flight mode of molten droplets showed by Chen et al. [11]. As a result, it provides heat input and distortions of the specimens. Therefore, it is usually applied for thin plates [12] and frequently for low dilution cladding

according to Pickin et al. [13]. Recently, CMT is frequently used for the wire arc additive manufacturing (WAAM) process and showed perspective results for aluminum alloys, e.g. for AA-6xxx [14]; AA-1xxx [15]; AA-2xxx [16]; and AA-5xxx [17]. It is also expanding for different materials, e.g. for tool steel [18], Cr-Ni steel [19], and Ni-based superalloys [20].

In the present work, dry hyperbaric welding of HSLA steel was applied in bead-on-plate configuration by utilizing CMT arc mode under different ambient pressures and with the use of two different filler wires. The effect of ambient pressure on weld bead geometry and cooling rates was established. Explanation of increasing penetration depth with increase of ambient pressure was described through dimensionless numbers and results are consistent with those of other researchers. The microstructure formation was studied based on simulated thermal cycles and characteristics of non-metallic inclusions (NMIs). The effect of ambient pressure on melt flow characteristics was investigated analytically. It will be shown that the experimental results are in good agreement with numerically simulated results.

2. Methodology

2.1. Equipment and materials

Bead-on-plate (BOP) welding was performed by GMAW process using a 15 mm thick X70 high strength low alloy (HSLA) steel. The arc torch was almost perpendicular (86-87°) to the plate surface. An illustration of the setup is schematically shown in **Fig. 1**. The GMAW equipment was a Fronius (TPS450x3, 200 V OCV) power source

with available CMT arc mode. The electrical data (current and voltage) of the arc were recorded. The constant process parameters are listed in **Table 1**.

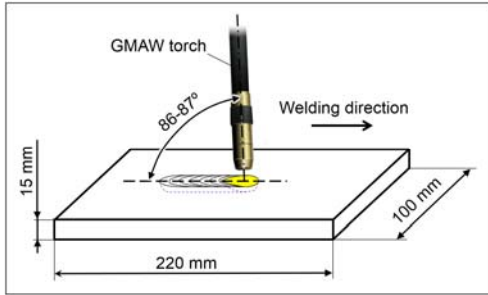The base plates were cut to dimensions of 220 mm × 100 mm × 15 mm with the welding direction parallel to the rolling direction. The plate and filler wire chemical composition and mechanical properties are presented in **Table 2** and **Table 3** respectively.

Fig. 1. Dry hyperbaric GMAW experimental setup

Table 1. Constant geometrical and process parameters

Parameter	Value
Travel speed (v_t)	0.6 m/min
Contact-tip-to-distance (CTWD)	12 ± 0.5 mm
Shielding gas composition	Argon
Shielding gas flow rate*	20 L/min

* for experiments at 1 bar ambient pressure

Table 2. Chemical composition (wt.%) of base plate and filler wires. Iron (Fe) in balance

Material	C	Si	Mn	P	S	Al	Ni
Base metal*	0.047	0.10	1.74	0.09	0.001	0.05	0.24
Wire-1	0.060	0.40	1.25	0.007	0.010	0.018	0.43
Wire-2	0.060	0.35	1.41	0.011	0.017	-	1.48

* Nb, Cr, Mo, Cu, Ti and V present in small amounts

Table 3. Mechanical properties of base plate and filler wires

Material	Yield strength, $R_{p0.2}$ (N/mm^2)	Ultimate tensile strength, R_m (N/mm^2)	Break elongation, ε (%)
Base metal	540	670	27
Wire-1	612	673	20
Wire-2	518 (min. 460)	598 (min. 530)	31 (min. 20)

2.2. Variables

The GMAW parameters as voltage, frequency, current, background current and pulse time were set according to the synergetic lines for the specific program used. For process stability, the synergetic line means that the filler wire feed rate (*WFR*) was controlled by pre-set arc current and voltage.

The heat input is calculated according to the following formula:

$$Q_{in} = \frac{60 \cdot I \cdot U \cdot \eta}{1000 \cdot v_t} \tag{1}$$

Experiments were carried out in a pressurized chamber filled with 99.995% argon. Before welding, the chamber was depressurized in order to

4

remove ambient oxygen. Shielding gas was not supplied by the GMAW torch in the chamber with exception for the weld deposited at 1 bar.

Two different metal-cored filler wires were applied. Wire-1 (ESAB Coreweld HBQ) with 1.0 mm in diameter and wire-2 (Kobelco TrustArc MX-A55T) with 1.2 mm in diameter. Wire-1 was specifically developed for the dry hyperbaric welding purposes with additional oxygen content (> 450 ppm) in deposited weld according to Woodward et al. [21] in order to provide higher acicular ferrite content based on Bhadeshia and Honeycombe [22].

Their chemical composition and mechanical properties are shown in **Table 2** and **Table 3** respectively. The welding parameters are presented in **Table 4** for each tested wire. For wire-2, a reduced *WFR* was used to achieve similar heat input and compare its effect on process stability and weld geometry.

Table 4. Welding parameters used in experiments. Current and voltage are average values

Ambient pressure (bar)	*WFR* (m/min)	*I*	*U*	Q_{in}
Wire-1				
1	10	199	20.0	0.32
17	10	198	26.2	0.42
35	10	205	26.3	0.43
Wire-2				
1	8	264	19.9	0.42
17	8	274	24.5	0.54
35	8	272	23.5	0.51

2.3. Analytical and mathematical formulation

The effect of pressure is discussed in terms of weld bead appearances using extracted macrosections. Thus, an analytical (qualitative and quantitative) approach is applied. Subsequently, a developed FEA was used to confirm the analytical approach. The logical sequence and methodology are shown in **Fig. 2**. The physical assumptions of the arc welding process is taken from DebRoy and David [23] as a theoretical base for acting forces in weld pool and from Tanaka and Lowke [24] including effect of the arc physics. The arc plasma gas drag (shear) force is neglected since there is no shielding gas supply in the hyperbaric chamber. Up to date, much work has been reported in GMAW arc simulation. However, not much work was done on simulation of dip-transfer mode.

Planckaert et al. [25] made a simple model of dip-transfer GMAW in CO_2 shielding gas and showed good agreement with experimental observation by high speed imaging with active contour algorithm. However, the results are vague probably due to complex molten metal transfer and has limited applicability. Due to stronger requirements for productivity, numerical simulation of the dip-transfer mode did not receive further attention. Modelling of the arc physics is still under concern due to very high complexity. Moreover, the simulation of welding processes when filler wire is added, the complexity is increasing further since it can employ different arc modes (e.g. pulsed arc) having more process parameters (e.g. pulsing frequency, pulsing duration,

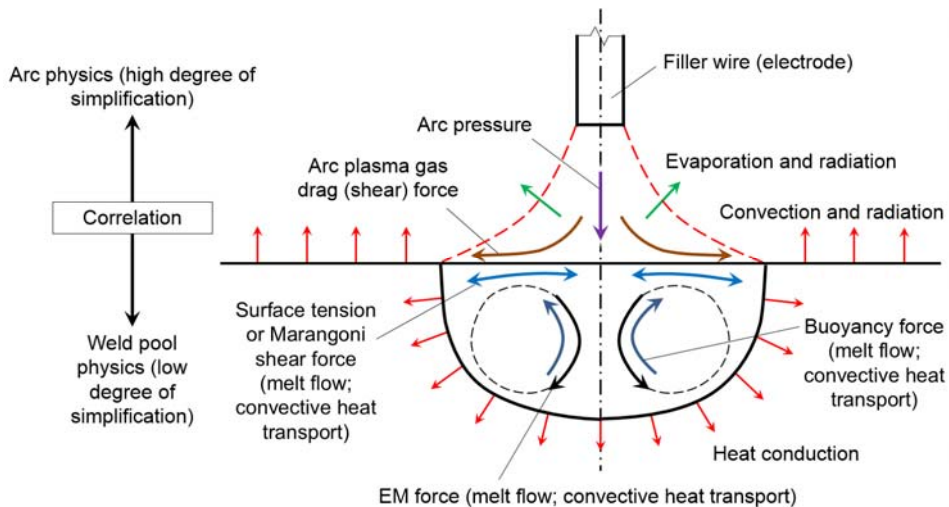pulsing shape etc.) with physics of the wire melting and impingement to the weld pool.

Fig. 2. Methodology of analytical studies of the forces and melt flows in weld pool

In this work, an assumption regarding surface active elements (sulphur and oxygen) is made, so that sulphur has no influence on surface tension since the content is very similar (see **Table 2**) and the same welding conditions are applied except for different ambient pressure. Sulphur content has significant effect on the surface tension and thus on penetration depth with significant change in weld pool morphology according to Pitschender et al. **[26]**. Oxygen content effect is investigated.

The isothermal thermo-physical parameters depending on the material state and were mainly taken from Zhang et al. **[27]**.

The thermal conductivity (k) and the specific heat (C_p) were chosen to be temperature dependent and presented graphically in **Fig. 3**. The non-isothermal physical parameters included in the model increase the reliability and complexity of the numerical modelling. These two are very critical parameters since it controls the width of the heat-affected zone for calibration, and geometry of the weld pool, and thus the accuracy of the model. For example, the peak included for specific heat at 600-800°C range occurs due to phase transformation phenomenon (ferrite to austenite) based on Li et al. **[28]**. It should be noted that these values are approximate since each steel has its unqiue specific heat values at elevated temperature according to Miettinen and Louhenkilpi **[29]**.
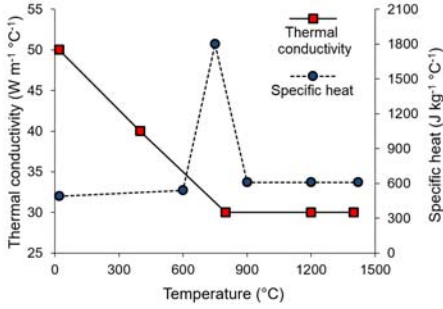
Fig. 3. Effect of temperature on thermal conductivity and specific heat

2.3.1. Dimensionless numbers analysis

Dimensionless numbers can be used to identify forces and specific parameters affecting weld pool morphology. They are based on the Buckingham π theorem [30] and compiled in **Table 5**.

Table 5. Dimensionless numbers

Dimensionless number	Formula	Description
Grashof number (Gr)	$Gr = \dfrac{g\beta L_B^3 \Delta T \rho_L^2}{\mu_L^2}$ [27]	The ratio of buoyance force to viscous force
Surface tension Reynolds number or Marangoni number (Ma)	$Ma = \dfrac{\rho_L L_B \Delta T |d\gamma / dT|}{\mu_L^2}$ [27]	The ratio of surface tension force, or Marangoni shear force, to viscous force
Electromagnetic Reynolds number (Re_m)	$Re_m = \dfrac{\rho_L \mu_m I^2}{4\pi^2 \mu_L^2}$ [27]	The ratio of electromagnetic force to viscous force
Peclet number (Pe)	$Pe = \dfrac{v_{max} L_P}{\alpha}$ [31] $Pe = \dfrac{v_{max} \rho_L C_p L_P}{k}$ [32]	Characterize heat transport of fluid by the relative magnitude of convective heat transfer to conductive heat transfer
Prandtl number (Pr)	$Pr = \dfrac{v_d}{\alpha}$ [33] $Pr = \dfrac{C_p \mu_d}{k}$ [30]	Characterize viscous (momentum) diffusion to thermal diffusion rate

2.3.2. Numerical modelling

The modelling was performed by the commercial ABAQUS 6.14 software. The numerical approach was solved by using transient heat transfer model with DFLUX subroutine programmed in Fortran language. In the model, the effects which are in computational fluid dynamics (CFD) are excluded: physical forces acting in the weld pool and their effects on melt flow, vaporization effects, weld pool deformations, arc and shielding gas pressure effects, filler wire mass addition etc. The model also excludes arc pulsing effects, i.e. average constant values. In the numerical

modelling, the weld bead reinforcement was excluded since it is not an area of interest and the model is simplified for the purpose of reduction in computational time.

The non-linear law of heat conduction according to Fourier's law (analogous to the Fick's law) has the following partial differential equation to be solved:

$$\frac{\partial}{\partial x}\left(k\frac{\partial T}{\partial x}\right) + \frac{\partial}{\partial y}\left(k\frac{\partial T}{\partial y}\right) + \frac{\partial}{\partial z}\left(k\frac{\partial T}{\partial z}\right) + \dot{Q}(x,y,z,t) = \rho C_p \frac{\partial T}{\partial t} \tag{2}$$

The 3D Goldak double ellipsoidal volumetric heat source Q_1 (**Eq. 3**) was used in combination with a 2D Gausian surface heat source model Q_2 (**Eq. 4**) based on Goldak and Akhlaghi [34].

$$Q_1 = q_f + q_r = \frac{6\sqrt{3}f_X UI\eta}{abc_X\pi\sqrt{\pi}}\exp\left(-\frac{3x^2}{a^2}\right)\exp\left(-\frac{3(y-vt)^2}{b^2}\right)\exp\left(-\frac{3z^2}{c_X^2}\right) \tag{3}$$

Here, the front quadrant power distribution is q_f and the rear is q_r. f_X is the fraction of heat deposited in the front ($f_{f1,2}$) and rear ($f_{r1,2}$) quadrants (with the sum equal to 2) and assumed to be equal to 1.5 and 0.5 respectively. The parameter a represents the arc weld pool width (mm), b denotes depth (mm) of the arc heat source, and c_X is front ($c_{f1,2}$) and rear ($c_{r1,2}$) pool length (mm) respectively.

$$Q_2 = \frac{P}{\pi r^2}\exp\left(-\frac{2(x^2+y^2)}{r^2}\right) \tag{4}$$

As a result, the volumetric heat source and the surface heat flux were combined: $Q_t = Q_1 + Q_2$.

The model involves adjustment of the source parameters (a, b, c_X, r) similarly to the modelling procedure by Aarbogh et al. [35] (two Goldak double ellipsoids and Gaussian surface) and Azar et al. [36] (two Goldak double ellipsoids) for dry hyperbaric welding applications. In the latter case, the

model is calibrated by top view of the weld bead and the same was done in this work in order to provide reliable model and thermal cycles. Azar [37] proposed a more advanced CMT model.

The model also includes the latent heat of fusion corresponding to the thermal effect of the solid-to-liquid phase transformation which makes the heat transfer highly non-linear and complex. This may, in turn, result in an increase of enthaphy (see **Eg. 5**) or energy release during solidifcation in order to increase reliability of the model since it can accurately simulate V-shape (weld pool). Mass proportion of molten material is expressed by **Eq. 6**.

$$H = \rho C_p T + \rho H_L f \tag{5}$$

$$f = \begin{cases} 0 & T < T_S \\ \dfrac{T-T_S}{T_L-T_S} & T_S \le T \le T_L \\ 1 & T > T_L \end{cases} \tag{6}$$

The model consisted of 349050 finite elements (linear hexagonal eight node DC3D8) with finer mesh near the weld centerline and coarser mesh away from the weld centerline.

A thermal boundary condition (**Eq. 7**) was applied to the top surface where the arc is acting taking into account the surface-to-ambient radiation and natural convection with ambient **[38]**:

$$Q_t(x,y,z,t) = -k\nabla T \cdot n = -k\frac{\partial T}{\partial n} = h_c(T - T_0) + \varepsilon\sigma(T^4 - T_0^4) \tag{7}$$

2.4. Metallurgical characterization

Transversal cross sections were cut from each weld and prepared for metallographic examination using standard preparation techniques (grinding, polishing and etching with 2% Nital). The welds were then examined with optical microscopy to assess the fraction of different microstructural constituents according to EN ISO 17639:2003. For CGHAZ studies, the area was selected as 1/2 of the maximum penetration depth (d_{max}), see **Fig. 4**.

For study of NMIs, the non-etched polished samples were inspected by optical microscope and scanning electron microscopy (SEM) with backscattering mode. Energy-dispersive X-ray spectroscopy (EDS) mapping was performed to investigate chemical composition of NMIs.

Due to small size of NMIs, large size and heterogeneous nature of weld joint, only a small area was covered. In order to build reasonably reliable statistical characterization of NMIs, four samples were selected from the center of welded joint. This provides 0.004984 mm^2 of inspected area, which was extrapolated to 1 mm^2 area by multiplication of 200.

Microhardness measurements were performed according to EN ISO 9015-2:2016 based on individual indentations with 500 gf load corresponding to HV$_{0.5}$.
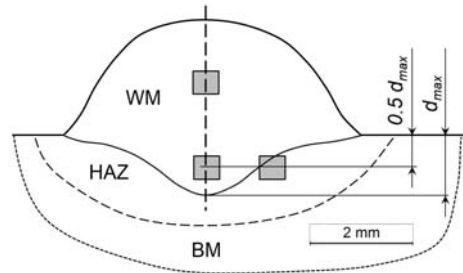

Fig. 4. Study and analysis plan of the welded joint

3. Results and discussion

3.1. Effect of pressure on process stability

Welding performed with the CMT arc mode at atmospheric pressure (1 bar) was stable based on a harmonic (or consistent) arc current and voltage response waveform pattern (**Fig. 5**a,b), and uniform weld bead (**Fig. 6**a,b) for both wires. Electrical data acquisition (5 kHz sampling was used) during processing revealed distinctive waveforms due to different wire diameters, thus different CMT synergy lines or program was used. As a result, the arc physics might be affected with subsequent changes in its synergy line or behavior.
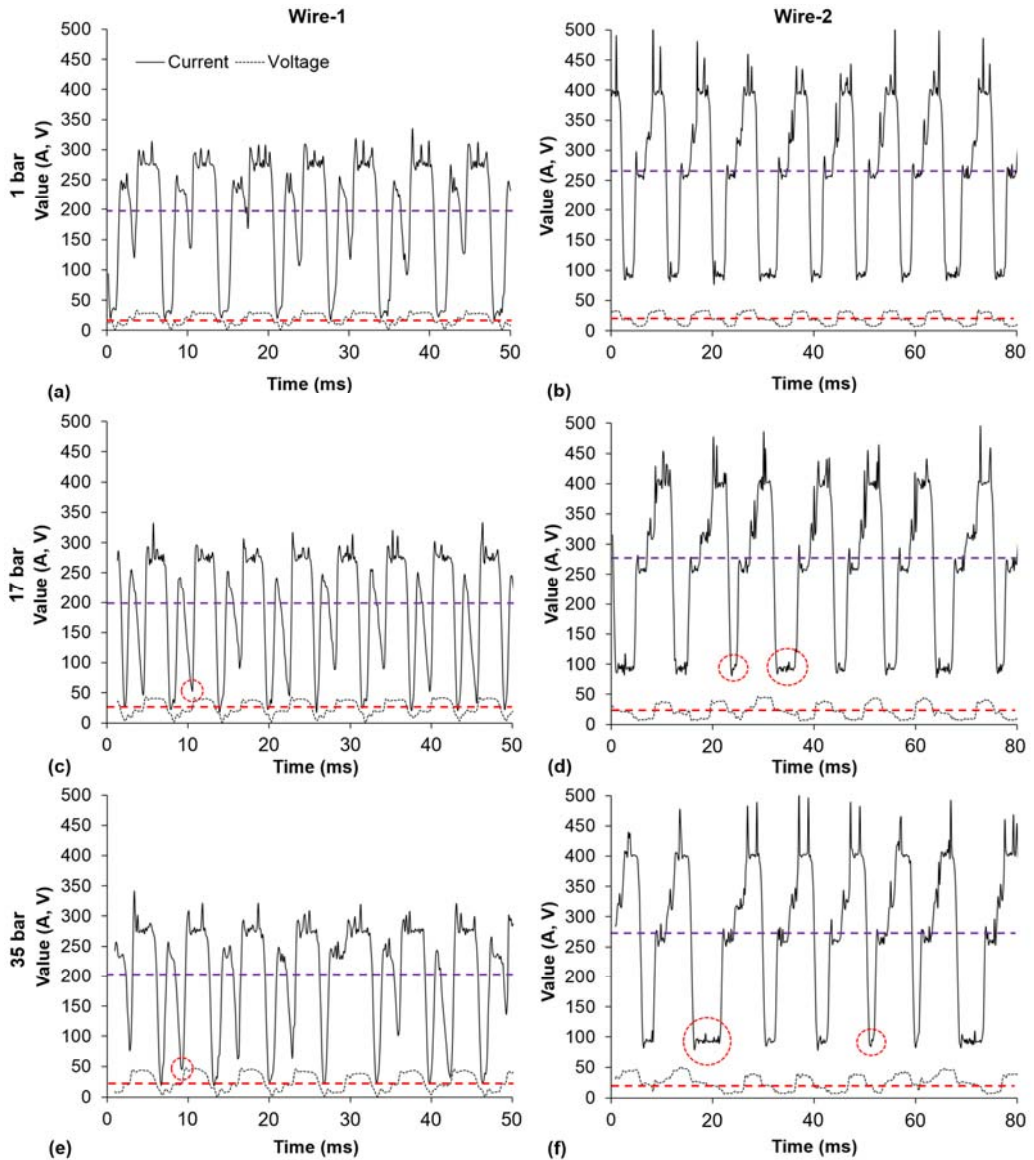
Fig. 5. Volt-ampere characteristics at different ambient pressures. Mean values represented by dashed lines

At increased pressure, a slight spattering occurred, and current waveforms had fluctuations (**Fig. 5**c-f). A similar trend is reported by Azar et al. **[39]** up to 250 bar and later by Ofem et al. **[6]** up to 200 bar. Specifically, it concerns fluctuation at the lower amplitude of the current during *wait stage* (indicated by a dashed red circle in **Fig. 5**c,e) indicating a destabilization of CMT transfer mode in case of wire-1. This fluctuation might be related to the change of the melt pool height, thus different times for pushing the wire into the weld pool. In case of wire-2,

10

the wait stage is very short and is probably related to the high *WFR*. A non-consistent duration at the *detachment stage* of the wire appears (indicated by a dashed red circle in **Fig. 5**d,f) which can be shorter or longer. Such behavior shows that retraction times are different. This indicates that the weld pool height is changing and affected by the ambient pressure.

Possibly, the arc is wandering, and the process becomes less stable. However, compared to the conventional pulsed arc mode based on Enjo et al. **[40]**, spattering is substantially lower since there is no free flight droplets transfer and fluctuation is significantly lower showing that CMT transfer mode is more stable at higher ambient pressures. Therefore, higher quality of welds can be achieved. Based on the current and voltage waveforms (see **Fig. 5),** regardless of the wire chosen and CMT program, the average voltage is increasing significantly (~22% for both wires) with increasing pressure. By contrast, the current has a low increase (~3%) mainly at 35 bar for both wires (see **Table 4)**. At higher pressures, the arc is very likely to be compressed to smaller volumetric dimensions, since the arc minimizes the enhanced heat extraction losses at the outer regions by reducing its diameter according to Nixon **[8]**. Therefore, the arc has higher current density with higher brightness. Another explanation could be that the ionization potential of the shielding gas is increasing at higher ambient pressures according to Nixon **[8]**. Therefore, higher voltage is required and subsequently adjusted by the welding power source in order to ionize the gas in the arc column, with metal vapor, to keep it stable.

According to the classic theory of welding, an increase in voltage produces wider welds during constant arc length **[41]**. When the arc length increases, the voltage will also increase. However, this also depends on the arc current range **[42]**. The arc length variation was not confirmed since no camera was used. However, based on previous research **[40]** in the case of constant arc length in the MIG process under similar conditions, the arc voltage behaved in the same manner.

3.2. *Effect of pressure on welded joint geometry*

Macrographs of the welded joints are shown in **Fig. 7**. Various resulting dimensions are compiled for wire-1 and wire-2 in **Fig. 8**a and **Fig. 8**b respectively. The increase of ambient pressure affects the weld pool morphology significantly. A change in the ambient pressure also affect wire metal deposition. Based on the results contained in **Fig. 5**, the pulse frequencies slightly increase at higher chamber pressure, especially at 17 bar in the case of wire-1. Therefore, higher deposition rate is achieved (see **Fig. 8**a). From **Fig. 8** it can be stated that there is noticeable increase of metal deposition at chamber pressure above 1 bar. This observation is related to the voltage and current increase providing enhanced melting of the wire. It concerns the peak currents, which are noticeably higher with increasing pressure. By contrast, in case of wire-2 there is lower metal deposition at 17 bar as well as reduced pulse frequencies. This implies that the pressure affects the filler wire deposition rates by adjusting the synergy curve.

Most noticeably, there is an increase of the penetration depth. There is a linear trend for wire-1 (see **Fig. 9**a), while a non-linear (logarithmic) trend

is found for wire-2 (**Fig. 9**b). A logarithmic trend can be related to the fact that metal deposition interferes with the dilution. An increased penetration depth may also affect the dilution rate, with the same difference between the wires as for penetration depth due to their interdependence for BOP welding. An increase of penetration depth is directly proportional (see **Fig. 9**) to the increase of heat input (see **Table 4**) or heat flux **[43]** which is mainly related to higher voltage. In fact, higher ambient pressure not always provides higher penetration depth **[39]**. This may be due to different welding conditions and process parameters.
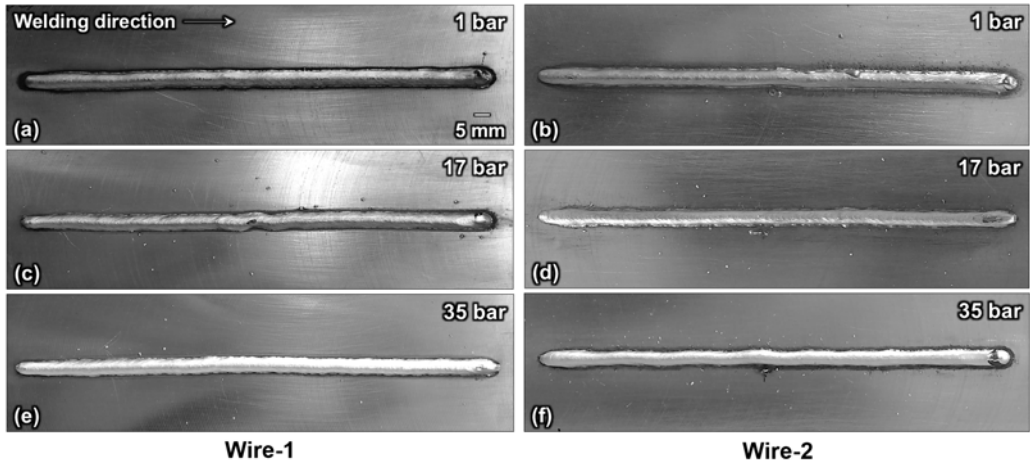
Fig. 6. Surface quality of deposited welds at different ambient pressure
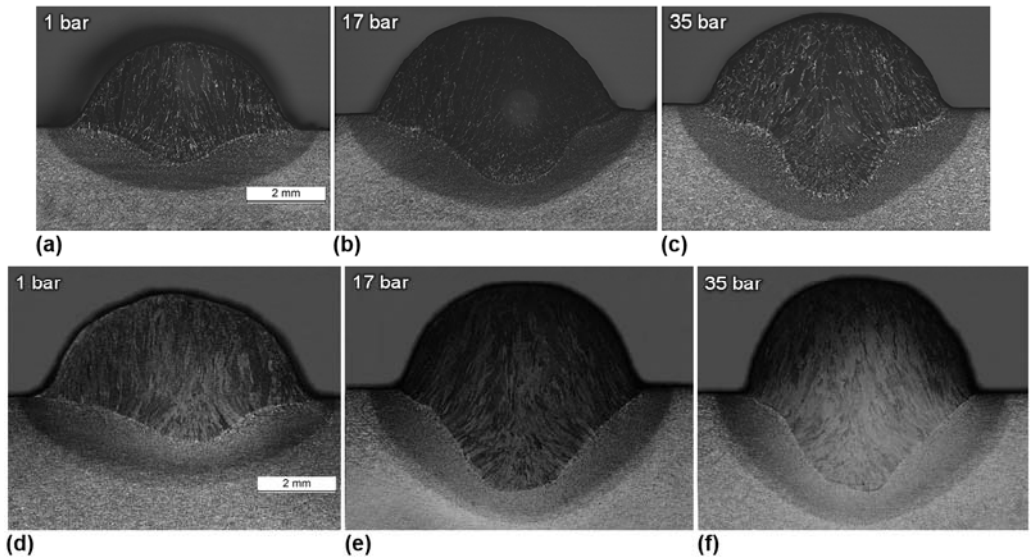
Fig. 7. Effect of ambient pressure on weld width and depth in case of wire-1: (a) 1 bar; (b) 17 bar; and (c) 35 bar; in case of wire-2: (d) 1 bar; (e) 17 bar; and (f) 35 bar
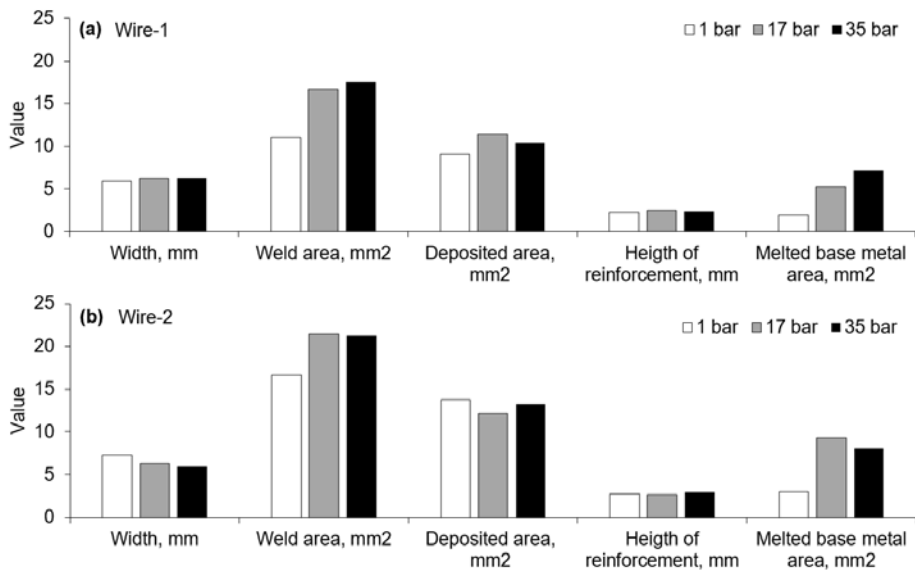
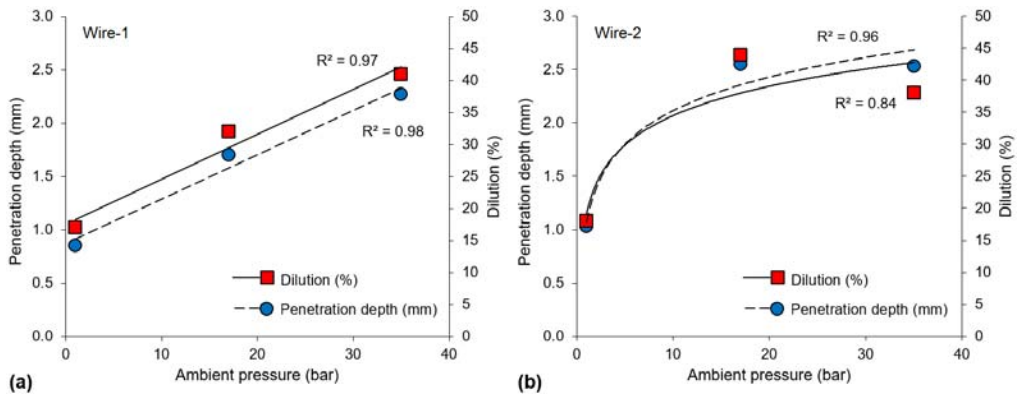**Fig. 8.** Resulting dimensions of deposited welds: (a) wire-1; and (b) wire-2

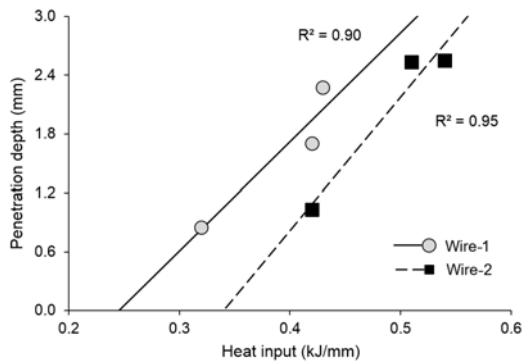**Fig. 9.** Effect of ambient pressure on penetration depth and dilution

Fig. 10. Effect of heat input on penetration depth

13

The proposed magnitudes and directions of the melt flow in the weld pool are schematically shown in **Fig. 11** in case of wire-1. This proposal is consistent with published results; 2D numerically estimated weld pool by tungsten inert gas (TIG) process with extended physics **[24]**, 2D of arc and laser weld pool calculation by **[30]**, 3D CFD based simulation of TIG process by **[43]**, and 3D CFD based simulation of finger shape evolution in GMAW by **[44]**. Based on **Fig. 7** where both wires showed similar bead appearance changes depending on change of ambient pressure. Thus, the same assumption is valid for wire-2 case. Arora et al. **[30]** showed convex weld shape in the center of the root of deposited welds with two vortexes, or recirculation loops of the melt flow. It was related to the melt flow dynamics

where higher convective heat transfer is achieved in the center providing melt vortex with inward flow direction. According to **[26]**, the melt flow velocity was increased by the factor of eight (from 4.8 cm/s to 37.4 cm/s) in the weld pool centerline when the laser power was tripled (up to 5.2 kW). Since similar arc power (see **Table 4**) was used, the same trend can be accepted for the current experiments.

All welds had convex shape of molten pool in the center, regardless ambient pressure. Therefore, there is two vortexes acting in the weld pool with pressure > 1 bar. Considering that CMT arc mode has no free-flight droplets with high kinetic energy to produce a *finger* convex shape at the center, thus the ambient pressure creates conditions for the finger-like shape penetration.
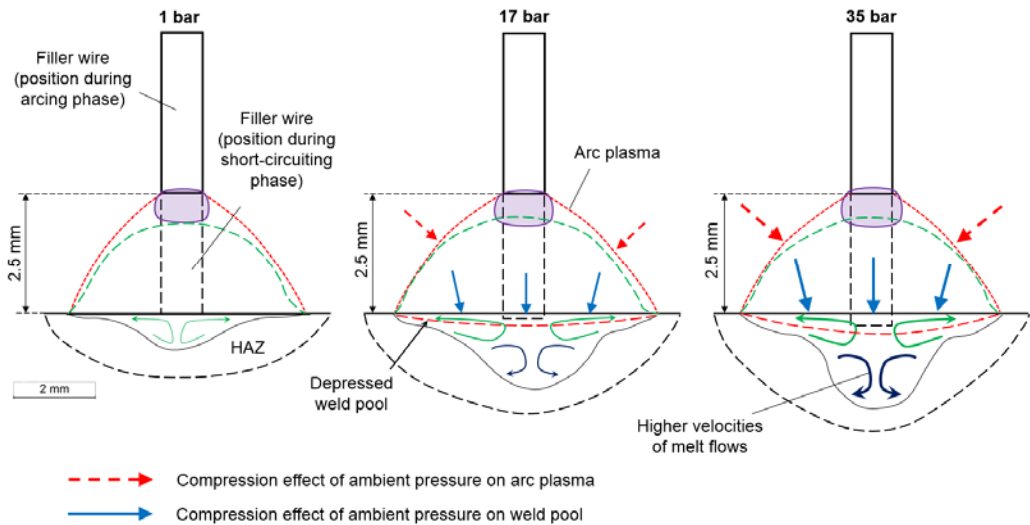

Fig. 11. Effect of ambient pressure on weld pool in case of wire-1

3.3. Dimensionless number analysis

A further analytical explanation on the increase of penetration depth can be done by means of dimensionless numbers. In this case, the parameters

presented in **Table 6** are accepted as constants and some of them dependent on the material state. L_B with ΔT are considered as variables since they are the most influential. L_B is measured directly from macrographs and ΔT is

calculated for each case depending on the heat input (**Fig. 12**). Subsequently, T_{wp} for 1 bar cases is assumed equal to 2100°C (for wire-1) and 2200°C (for wire-2) based on experimental observation of the weld pool temperature during processing **[45]**. T_{wp} values for > 1 bar are assumed linearly proportional to heat input (**Fig. 12**a). Notably, these values are amused to be closer to the plate surface in the weld pool regardless of the penetration depth. The boiling point of steel is assumed to be 2550°C. ΔT is the difference between maximum temperature in the weld pool (further denoted as T_{wp}) and solidus temperature (T_s) and given as logarithmic dependence on ambient pressure (**Fig. 12**b) derived from heat input. Naturally, with increase of ambient pressure, other parameters (μ_l, ρ_l, β and $d\gamma/dT$) also change within the specific location in the weld pool. However, since they are the function of ΔT and for the sake of simplicity, they are not included in the calculation.
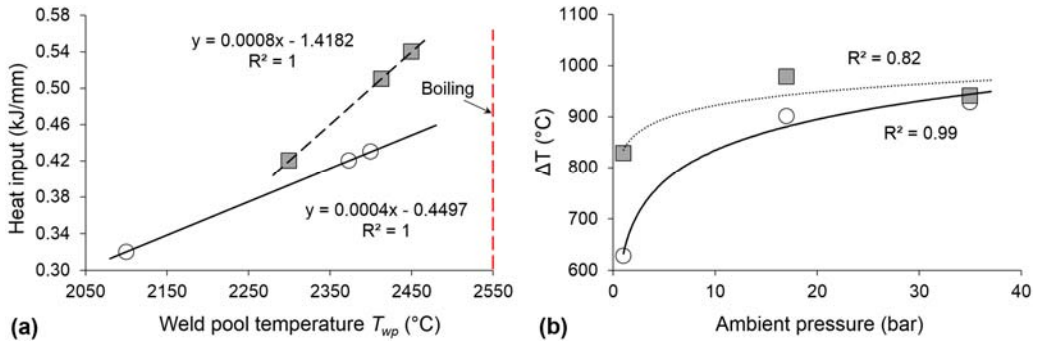

Fig. 12. Estimation of (a) T_{wp} near surface and (b) ΔT values

According to the estimated dimensionless numbers for wire-1 case (**Fig. 13**a), the Grashof number is raised by an increase in pressure, indicating that the buoyance force is slightly affected so that the convective heat transfer may increase. In case of wire-2 (**Fig. 13**b), the results are opposite since narrower welds are produced with an increased pressure, revealing low correlation of Grashof number with linear increase of penetration depth according to **Fig. 10**.

The Marangoni number shows identical trend as the Grashof number, see **Fig. 13**b. The Marangoni shear force is changing with increasing pressure and has contradictory results for the different wires. As a result, the Marangoni number shows low correlation with a linear increase of penetration depth. Therefore, the Marangoni shear stress has low influence on increasing penetration depth. The arc plasma drag force affects the Marangoni shear force since it is acting on the weld pool surface with its direction from the arc core towards the weld pool's edges (see **Fig. 2**). Therefore, the plasma drag force has no effect in a pressurized chamber since there is no shielding has used from the arc torch.

The electromagnetic force seems to be more relevant at 35 bar based on **Fig. 13**c. Possibly, an increase of current by 3%, has some effect on penetration depth in both cases, which is confirmed by **[24]**. In addition, the current increase might be significant

since it is significantly affecting the electromagnetic force according to **Eq. 8 [46]**. This equation is simplified and valid for both the radial and axial electromagnetic force (instead of R_1 the variation of height h is used in respect to z component, h-z). Since penetration depth linearly increasing with ambient pressure, the electromagnetic force has some correlation. It also significantly affected by the arc radii based on **Eq. 8**.

$$F_{EM} = -\frac{\mu_m I^2}{4\pi^2 R_2^2 R_1} \exp\left(-\frac{R_1^2}{2R_2^2}\right)\left[1 - \exp\left(-\frac{R_1^2}{2R_2^2}\right)\right]$$

(8)

At increasing ambient pressures the effective arc diameter tend to be reduced based on Nixon **[8]**, and it causes significant increase of electromagnetic force. It is very difficult to assess the anode and cathode spot (or arc) diameters, especially when alternate polarity is used depending on the stage for advanced CMT modes as recently studied by Guojin et al. **[47]**. So far, the diameters were not reported for such study case. However, it is possible that reduced arc radii are more effective than arc current increase under hyperbaric conditions.

Two other factors which affect the penetration depth are the depression of the weld pool due to higher ambient pressure (see **Fig. 11)**, and the arc pressure itself due to compression of the arc plasma. The latter also affects weld pool depression. This can additionally enhance melt flow magnitudes; velocity and appearance of the root melt vortex, and directions inward) for penetration depth increase. By numerical simulation, Cho et al. **[43]** proved that an increase of penetration depth (TIG process) was related to a higher arc pressure and a higher shielding gas flow rate. Their results can be equivalent to an increased ambient pressure on the weld pool as in the present experiments. However, in early studies by Lin and Eagar **[48]**, it was identified that arc pressure can cause narrow and deep penetration only at very high current increase (> 300 A). According to **Fig. 5**, peak currents increase with increasing ambient pressure and exceed the 300 A threshold. Similar to the electromagnetic force, the arc pressure is (P_A), also related to the effective radius of the arc according to the **Eq. 9 [49]**.

$$P_A = \frac{\mu_0 I^2}{8\pi}\left(1 + 2\ln\frac{R_2}{R_1}\right)$$

(9)

3.4. Numerical modelling results

The results from numerical simulation are shown in **Fig. 14**. The simulations for the 35 bar case are in good agreement with experimental results for both welding wires. The effect of pressure can be empirically included in the Goldak double ellipsoidal volumetric heat source as a function of the z-axis with adjustment of the heat source parameters. The model was calibrated based on several criteria: conformity with the fusion zone boundary, low temperature boundary of the subcritical heat-affected zone (which is assumed to be 750°C corresponding to A_1 line for low carbon steel based on Fairchild et al. **[50]**, thermocouple measurements, and the

top geometry of the weld bead. Subsequently, thermal cycles were extracted for the points of interest, at the top surface and $d_{max}/2$ at the weld centerline. The numerically estimated cooling rates, reported as $\Delta t_{8/5}$, seems to be reasonable since similar cooling rates (experimental and numerical) were reported by Azar et al. [7] which were in the range of ~1.2-1.5 s for welds under hyperbaric conditions (also up to 35 bar) with conventional pulsed arc mode. Based on the numerical simulation, the cooling rate

(a)

(b)

(c)

Fig. 13. Effect of ambient pressure on dimensionless numbers

($\Delta t_{8/5}$) is ~0.8-0.9 s for both wires at 35 bar. Notably, numerically estimated cooling rates might be slightly faster since the exact SCHAZ limit (in degrees) is unknown, thus the fastest possible cooling rate is given. For the pure CMT process under hyperbaric conditions, the cooling rate can be predicted (for bead-on-plate) calculated approximately by the following expression: $\Delta t_{8/5} \approx 2.2 \times Q_{in} \times 0.8$.

Notably, the thermal conductivity was reduced (by ~10%) for wire-1 since the HAZ is narrower and it can be related to different thermal properties of the wire due to different chemical composition. In addition, it has different CMT cycle, with slightly lower heat input, and that might also have an effect.
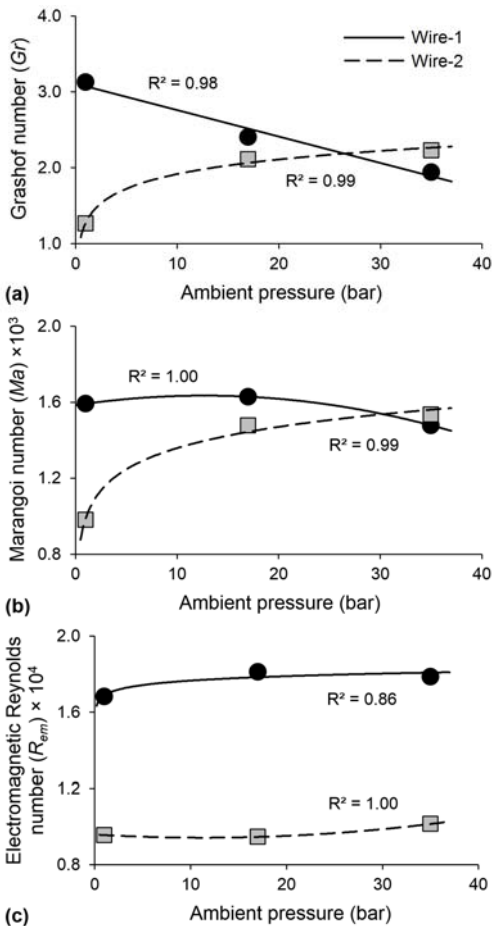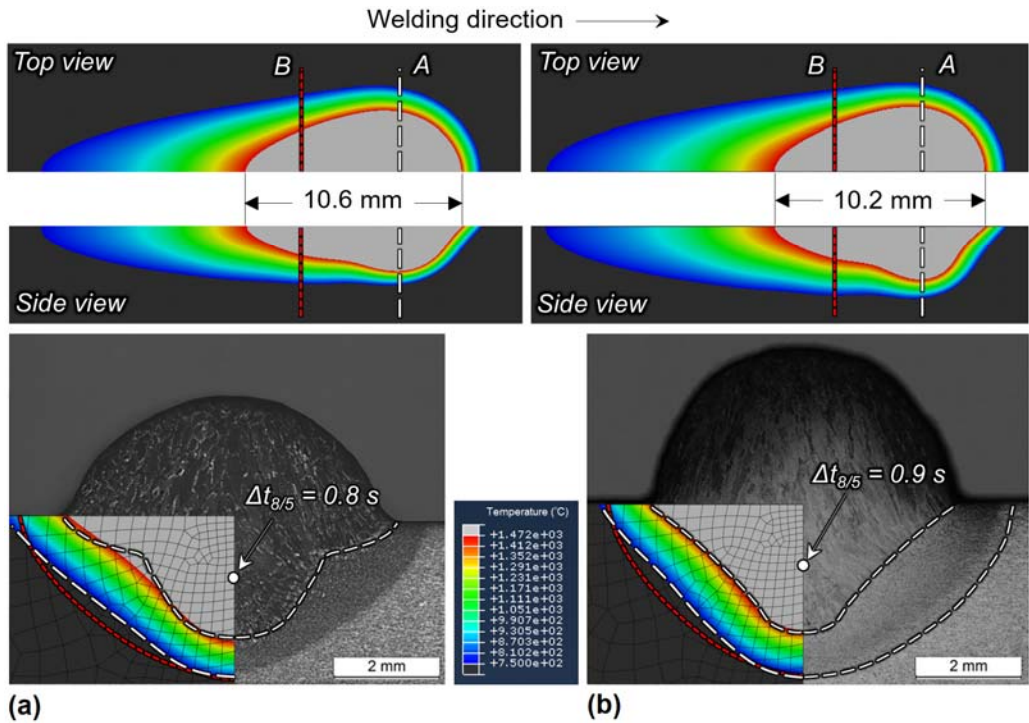
Fig. 14. Numerically simulated welded joints at 35 bar ambient pressure for (a) wire-1 and (b) wire-2

3.5. Metallurgical characterization

The two applied metal-cored wires have very different microstructure evolution in weld metal, see **Fig. 15** (high magnification) and **Fig. 16** (low magnification). Ambient pressure seems to have low effect on microstructure evolution due to similar heat input. In fact, the fine-grained AF was formed with much finer size than as-received base metal (**Fig. 16**d) for wire-1 welds. Thus, high toughness would be expected. Wire-1 produced much higher volume fraction of acicular ferrite than wire-2, > 70% and < 20% respectively. Along with the high volume fraction of AF, some primary WF, polygonal ferrite and grain boundary ferrite (or allotriomorphic) was also developed for wire-1. Therefore, it has lower

hardness with mean $HV_{0.5}$ of 287 (SD = 3.65). Accordingly, wire-1 has much higher potential in providing AF in weld metal even at very fast cooling rate. It may have a very high potential in application of deep and narrow welds made by laser-arc hybrid welding where high cooling rates ($\Delta t_{8/5}$ = 0.5-1.0 s) are involved in the root area based on Bunaziv et al. **[51]**. In addition, it has a certain potential for use in cladding or additive manufacturing purposes by the CMT arc mode, especially where high toughness (high volume fraction of AF) is required.

In case of wire-2, mainly bainite was formed. The ferritic plates (or grains) were more elongated (coarse AF) probably related to lower number of active NMIs and the growth of plates continues until they encounter an

18

obstacle (e.g. other growing plates or grain boundary). Moreover, it is possible that ferrite plate growth will stop when, combined with continuously decreasing temperature, the remaining austenite becomes sufficiently enriched with carbon decomposes to a ferrite-carbide aggregate. The detailed mechanism is described by Ricks et al. [52]. Such coarser AF more resembles intragranular Widmanstätten ferrite (IWF). In addition, lath martensite is formed in WM with wire-2, and the mean hardness was 350 $HV_{0.5}$ (SD standard deviation = 11.3). The cooling rate was similar for the two wires since wire-2 provided only slightly higher heat input.

The microstructure formed in CGHAZ (near fusion line, see **Fig. 16**c) mainly consisted of bainite and lath martensite. The mean hardness of 310 $HV_{0.5}$ (SD = 11.4, according to several random measurements) was similar for all welds produced due to minor variation in welding conditions. A slight difference in prior austenite grain size was observed with largest grain size found for the higher heat input.

The statistical characterization of NMIs is presented in **Fig. 17**. Due to similar cooling rates for both wires, the average diameter of inclusions (d_v) is similar. Therefore, d_v is not the main reason for higher AF formation in wire-1. However, it is generally admitted that with an increase of d_v, the nucleation of AF is higher. Based on Kluken and Grong [53] the average diameter of NMIs logarithmically increases with heat input and the mean diameter of inclusions is a function of $d_v = 0.35(\eta Q_{in})^{1/3}$. The results at 35 bar are: $d_v = 0.245$ and $d_v = 0.260$ for wire-1 and wire-2, respectively; smaller NMIs are formed since the cooling rate is evidently faster under hyperbaric

conditions using the CMT process compared to conventional pulsed arc wedling at atmosphetic pressure condition.

Higher amount of NMIs containing oxygen has higher potential for nucleation of AF based on Shim et al. [54] and Zhang et al. [55]. However, according to EDS mapping results (see **Fig. 18**) NMIs produced by wire-2 also had similar amount of oxygen as wire-1. Further, an inert gas fusion analysis (IGFA) was performed. The results showed that wire-1 had 520 ppm (regardless ambient pressure) compared to wire-2 which provided 760 ppm of oxygen. Moreover, more NMIs with composition of $(Ti)_xO$ and TiN were produced in wire-2, also being potent for AF nucleation. In general, both wires produced complex NMIs with Al_2O_3 as a core with MnS and TiN in the outer shell as described in [56]. Some simple (e.g. SiO_2) and complex silicates (e.g. $Mn_2 \cdot (Al_2O_3)_2 \cdot Si_5$ and/or $(Al_2O_3)_3 \cdot Si_2$) according to EDS mapping (see **Fig. 19**) developed in case of wire-1 which are potent nuclei for AF based on [57]. This partly explain why wire-1 provided much higher AF volume fraction.

The prior austenite grain size can be important for the AF formation due to its competitiveness with bainite formation according to Babu and Bhadeshia [58]. However, the prior austenite grain size for both cases is very similar due to the use of same base plate and similar heat input with subsequent cooling rate.

Wire-2 had higher nickel content and higher hardness, which demonstrates higher hardenability. The lower amount of AF may thus be due to excessive hardenability for the rapid cooling rate employed. The microstructure examination showed that this wire had low potency for grain

boundary ferrite formation along prior austenite grain boundaries. It strengthen the assumption of excessive hardenability. This observation may be the main reason for the lower AF volume fraction, providing favorable intergranular condition for bainite to form.
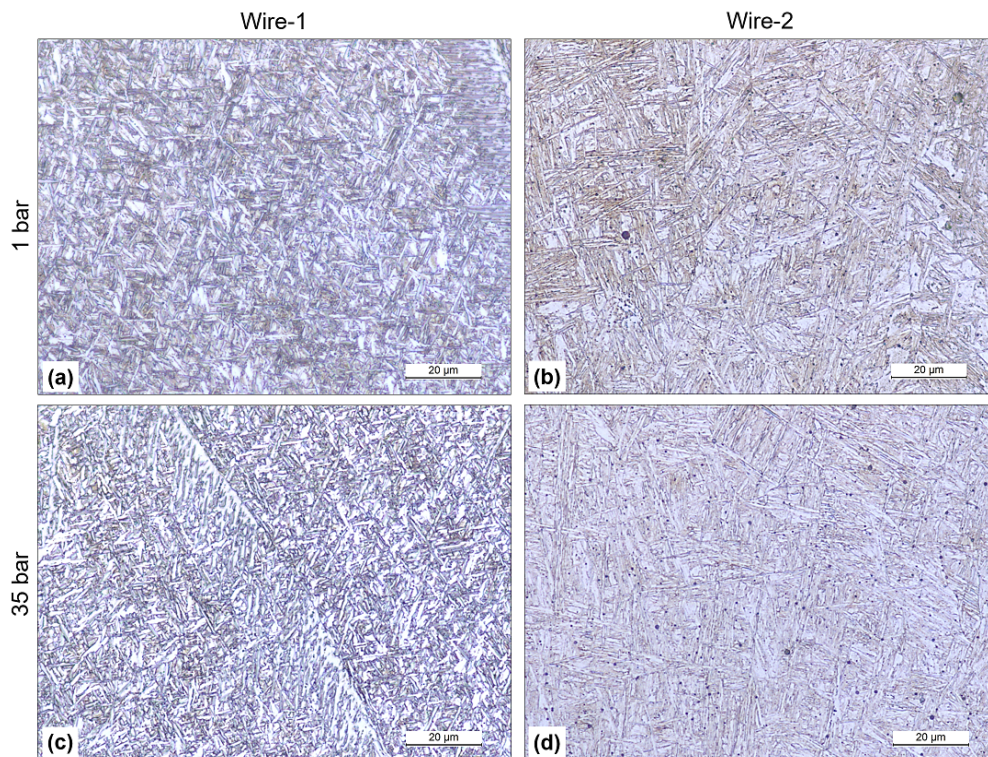

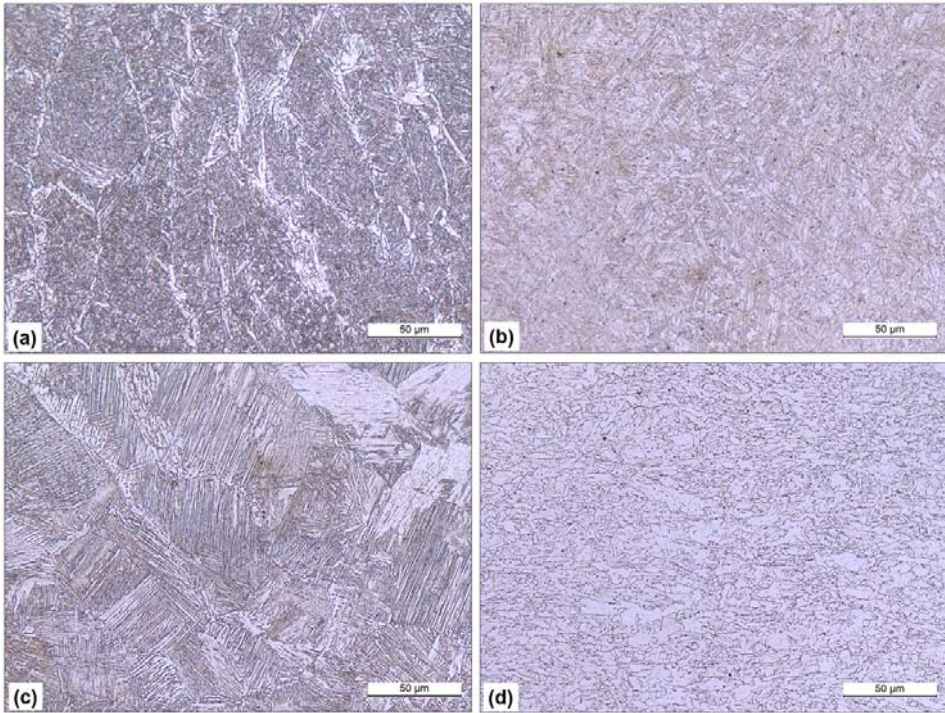**Fig. 15.** Optical micrographs of weld metal at different ambient pressure and filler wires

Fig. 16. Optical micrographs with lower magnification in (a) weld metal (35 bar, wire-1), (b) weld metal (35 bar, wire-2), (c) CGHAZ (1 bar, wire-1) compared to (d) base metal.
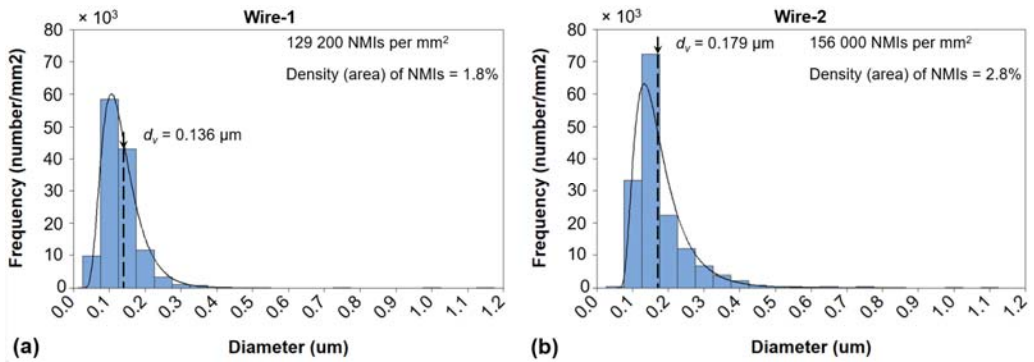

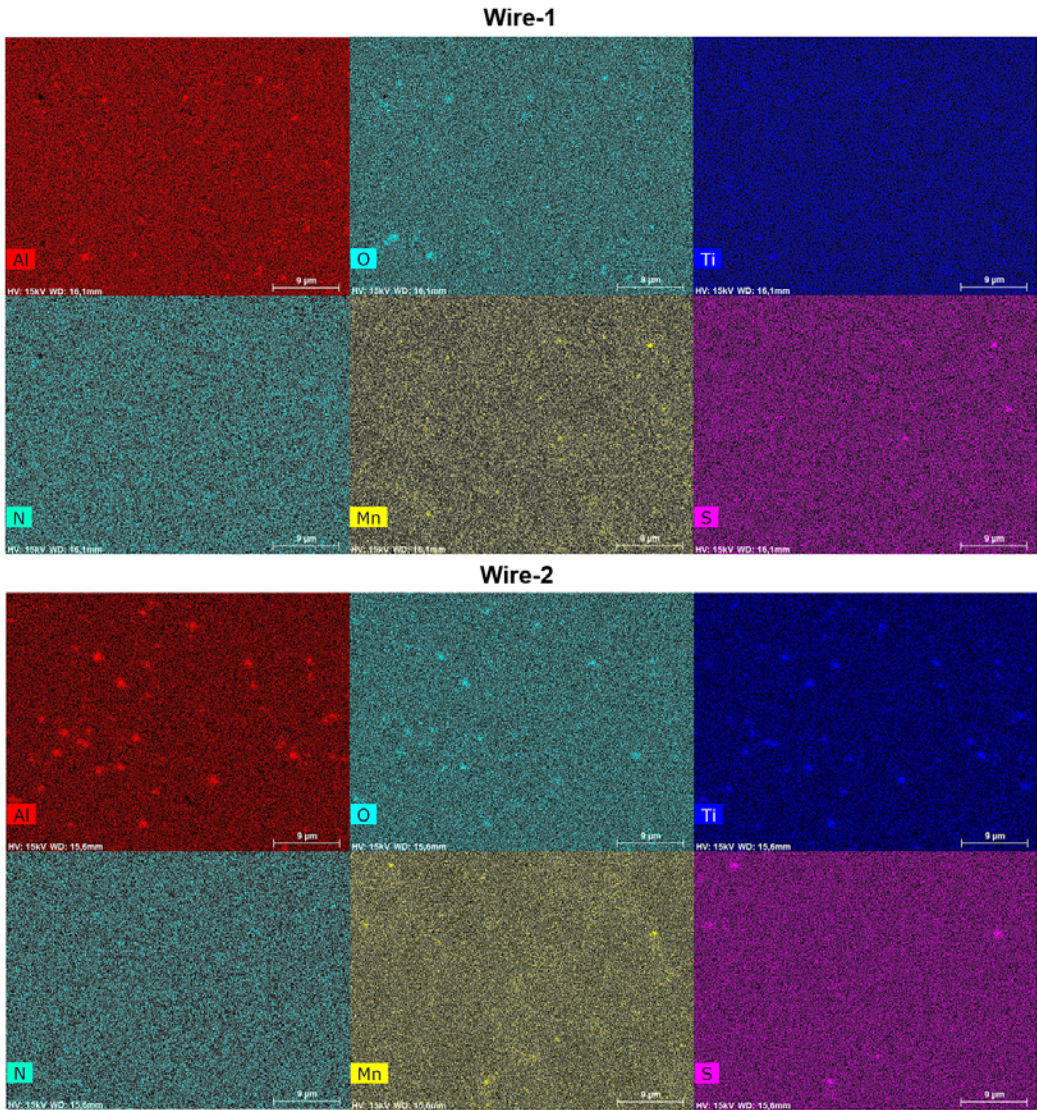**Fig. 17.** Statistical characterization of NMIs for (a) wire-1 and (b) wire-2

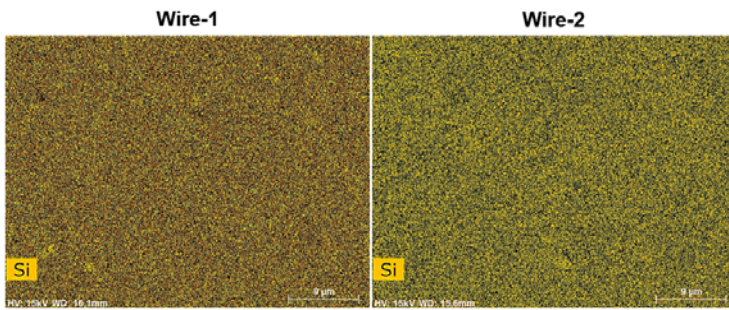**Fig. 18.** Chemical characterization of NMIs by EDS mapping

Fig. 19. Silicon content for different wires

4. Conclusions

Based on laboratory experiments and numerical analyses, the following conclusions can be drawn:

1) With increase of ambient pressure, the process stability deteriorates due to constricted arc conditions;

2) The penetration depth increases significantly with increasing ambient pressure which enhances melt flow magnitude (faster) and direction (inward);

3) The increased ambient pressure has low effect on the Marangoni force for enhancing penetration depth. The electromagnetic force with convective heat transport (faster melt flows) due to higher arc pressure is the most influencing factor for controlling weld geometry;

4) The filler wire with lower nickel and higher silica content provides higher volume fraction of acicular ferrite at any ambient pressure even though the amount and mean average size of non-metallic inclusions are lower. Therefore, this wire is more suitable for processes with faster cooling rates such as CMT.

Acknowledgements

References

1. Richardson, I.M.;N.J. Woodward;M.A. ArmstrongJ.O. Berge. *Developments in Dry Hyperbaric Welding*. in *3rd International Workshop on Stat-of-the-Art Science and Reliability of Underwater Welding and Inspection Technology*. 2010. Houston, Texas, USA

2. Hart, P.R., *A Study of non-consumable welding processes for diverless deepwater hyperbaric welding to 2500m water depth*. 1999, Cranfield University.

3. Akselsen, O.M.;R. Aune;H. FostervollA.S. Harsvoer, *Dry Hyperbaric Welding of Subsea Pipelines*. Welding Journal, 2006. **85**(6): p. 52-55.

4. Azar, A.S., *Dry Hyperbaric Gas Metal Arc Welding of Subsea Pipelines: Experiments and Modeling*, in *Department of Engineering Design and Materials*. 2012, Norwegian University of Science and Technology (NTNU): Trondheim, Norway.

5. Richardson, I.M.J.H. Nixon. *Deepwater Hyperbaric Welding – Initial Process Evaluation*. in *Proc. 7th International Conf. on Offshore and Polar Engineering (ISOPE)*. 1997. Honolulu, Hawaii, USA.

6. Ofem, U.;S. Ganguly;S. WilliamsN. Woodward, *Investigation of Thermal Cycle and Metallurgical Characteristics of Hyperbaric Gas Metal Arc Welding* in *International Journal of Offshore and Polar Engineering (ISOPE)*. 2014, International Society of Offshore and Polar Engineers. p. 207-212.

7. Azar, A.S.;O.M. AkselsenH. Fostervoll. *Prediction of the Thermal Cycles in Dry*

    Hyperbaric GMA Welding Using Partial Differential Heat Transfer Equations in *International conference; 9th, Trends in welding research; 2012; Chicago, IL*. 2012. Materials Park, OH ASM International

8.   Nixon, J.H., *Underwater Repair Technology* 1995: Gulf Professional Publishing 108.

9.   Richardson, I.M.J.H. Nixon. *Open Arc Pulsed Current GMAW: Application to Hyperbaric Welding Operations*. in *ASM International Welding Conference*. 1985. Toronto, Canada.

10.   Schörghuber, M., *Inventor cold-metal-transfer welding process and welding installation patent* 2005, US20090026188 A1.

11.   Chen, M.;D. ZhangC. Wu, *Current waveform effects on CMT welding of mild steel*. Journal of Materials Processing Technology, 2017. **243**: p. 395-404.

12.   Feng, J.;H. ZhangP. He, *The CMT short-circuiting metal transfer process and its use in thin aluminium sheets welding*. Materials & Design, 2009. **30**(5): p. 1850-1852.

13.   Pickin, C.G.;S.W. WilliamsM. Lunt, *Characterisation of the cold metal transfer (CMT) process and its application for low dilution cladding*. Journal of Materials Processing Technology, 2011. **211**(3): p. 496-502.

14.   Wang, P.;S. Hu;J. ShenY. Liang, *Characterization the contribution and limitation of the characteristic processing parameters in cold metal transfer deposition of an Al alloy*. Journal of Materials Processing Technology, 2017. **245**: p. 122-133.

15.   Zhang, C.;Y. Li;M. GaoX. Zeng, *Wire arc additive manufacturing of Al-6Mg alloy using variable polarity cold metal transfer arc as power source*. Materials Science and Engineering: A, 2018. **711**: p. 415-423.

16.   Ryan, E.M.;T.J. Sabin;J.F. WattsM.J. Whiting, *The influence of build parameters and wire batch on porosity of wire and arc additive manufactured aluminium alloy 2319*. Journal of Materials Processing Technology, 2018. **262**: p. 577-584.

17.   Zhang, B.;C. Wang;Z. Wang;L. ZhangQ. Gao, *Microstructure and properties of Al alloy ER5183 deposited by variable polarity cold metal transfer*. Journal of Materials Processing Technology, 2019. **267**: p. 167-176.

18.   Ali, Y.;P. Henckell;J. Hildebrand;J. Reimann;J.P. BergmannS. Barnikol-Oettler, *Wire arc additive manufacturing of hot work tool steel with CMT process*. Journal of Materials Processing Technology, 2019. **269**: p. 109-116.

19.   Zhang, X.;Q. Zhou;K. Wang;Y. Peng;J. Ding;J. KongS. Williams, *Study on microstructure and tensile properties of high nitrogen Cr-Mn steel processed by CMT wire and arc additive manufacturing*. Materials & Design, 2019. **166**: p. 107611.

20.   Xu, X.;J. Ding;S. GangulyS. Williams, *Investigation of process factors affecting mechanical properties of INCONEL 718 superalloy in wire + arc additive manufacture process*. Journal of Materials Processing Technology, 2019. **265**: p. 201-209.

21.   Woodward, N.J.;H. Fostervoll;O.M. Akselsen;C.H. Ahlen;J.O. BergeM. Armstrong. *Inconel 625 Performance as Hyperbaric GMA Welding Consumable for Diverless Retrofit Tee Hot Tap Applications*. in *International Society of Offshore*

and Polar Engineers (ISOPE). 2007. Lisbon, Portugal.

22. Bhadeshia, H.K.D.H.R.W.K. Honeycombe, *Steels: Microstructure and Properties*. 3rd ed. 2006: Butterworth-Heinemann.

23. DebRoy, T.S.A. David, *Physical processes in fusion welding.* Rev. Mod. Phys., 1995. **67**(1): p. 85-112.

24. Tanaka, M.J.J. Lowke, *Predictions of weld pool profiles using plasma physics.* Journal of Physics D: Applied Physics, 2007. **40**(1): p. R1.

25. Planckaert, J.-P.;E.-H. Djermoune;D. Brie;F. BriandF. Richard, *Modeling of MIG/MAG welding with experimental validation using an active contour algorithm applied on high speed movies.* Applied Mathematical Modelling, 2010. **34**(4): p. 1004-1020.

26. Pitscheneder, W.;T. DebRoy;K. MundraR. Ebner, *Role of Sulfur and Processing Variables on the Temporal Evolution of Weld Pool Geometry during Multikilowatt Laser Beam Welding of Steels.* Welding Journal, 1996. **75**: p. 71-80.

27. Zhang, W.;C.-H. KimT. DebRoy, *Heat and fluid flow in complex joints during gas metal arc welding—Part II: Application to fillet welding of mild steel.* Journal of Applied Physics, 2004. **95**(9): p. 5220-5229.

28. Li, M.;J.A. Brooks;D.G. AtteridgeW.D. Porter, *Thermophysical property measurements on low alloy high strength carbon steels.* Scripta Materialia, 1997. **36**(12): p. 1353-1359.

29. Miettinen, J.S. Louhenkilpi, *Calculation of thermophysical properties of carbon and low alloyed steels for modeling of solidification processes.* Metallurgical and Materials Transactions B, 1994. **25**(6): p. 909-916.

30. Arora, A.;G.G. RoyT. DebRoy, *Unusual wavy weld pool boundary from dimensional analysis.* Scripta Materialia, 2009. **60**(2): p. 68-71.

31. DebRoy, T.;H.L. Wei;J.S. Zuback;T. Mukherjee;J.W. Elmer;J.O. Milewski;A.M. Beese;A. Wilson-Heid;A. DeW. Zhang, *Additive manufacturing of metallic components – Process, structure and properties.* Progress in Materials Science, 2018. **92**: p. 112-224.

32. Mishra, S.;T.J. Lienert;M.Q. JohnsonT. DebRoy, *An experimental and theoretical study of gas tungsten arc welding of stainless steel plates with different sulfur concentrations.* Acta Materialia, 2008. **56**(9): p. 2133-2146.

33. Robert, A.T. Debroy, *Geometry of laser spot welds from dimensionless numbers.* Metallurgical and Materials Transactions B, 2001. **32**(5): p. 941-947.

34. Goldak, J.M. Akhlaghi, *Computational Welding Mechanics*. 2005: Springer.

35. Aarbogh, H.M.;M. Hamide;H.G. Fjær;A. MoM. Bellet, *Experimental validation of finite element codes for welding deformations.* Journal of Materials Processing Technology, 2010. **210**(13): p. 1681-1689.

36. Azar, A.S.;S.K. ÅsO.M. Akselsen, *Determination of welding heat source parameters from actual bead shape.* Computational Materials Science, 2012. **54**: p. 176-182.

37. Azar, A.S., *A heat source model for cold metal transfer (CMT) welding.* Journal of Thermal

Analysis and Calorimetry, 2015. **122**(2): p. 741-746.

38. Lindgren, L.-E., *Computational Welding Mechanics*. 2007, Woodhead Publishing p. 47-53.

39. Azar, A.S.;N. Woodward;H. FostervollO.M. Akselsen, *Statistical analysis of the arc behavior in dry hyperbaric GMA welding from 1 to 250 bar.* Journal of Materials Processing Technology, 2012. **212**(1): p. 211-219.

40. Enjo, T.;Y. Kikuchi;H. HorinouchiH. Ueda, *MIG Welding under High Pressure Arc Arc Atmosphere.* Transaction of JWRI, 1987. **16**(2): p. 267-276.

41. Weman, K., *MIG Welding Guide*. 2006: CRC Press.

42. Dos Santos, E.B.F.;L.H. Kuroiwa;A.F.C. Ferreira;R. PistorA.P. Gerlich, *On the Visualization of Gas Metal Arc Welding Plasma and the Relationship Between Arc Length and Voltage.* Appl. Sci., 2017. **7**(5).

43. Cho, D.W.;S.H. LeeS.J. Na, *Characterization of welding arc and weld pool formation in vacuum gas hollow tungsten arc welding.* Journal of Materials Processing Technology, 2013. **213**(2): p. 143-152.

44. Cheon, J.;D.V. KiranS.-J. Na, *CFD based visualization of the finger shaped evolution in the gas metal arc welding process.* International Journal of Heat and Mass Transfer, 2016. **97**: p. 1-14.

45. Kozakov, R.;H. Schöpp;G. Gött;A. Sperl;G. WilhelmD. Uhrlandt, *Weld pool temperatures of steel S235 while applying a controlled short-circuit gas metal arc welding process and various shielding gases.* Journal of Physics D: Applied Physics, 2013. **46**(47): p. 475501.

46. Tsao, K.C.C.S. Wu, *Fluid Flow and Heat Transfer in GMA Weld Pools.* Welding Journal, 1988. **67**: p. 70-76.

47. Guojin, L.;Z. Peilei;W. Xi;N. Yunpeng;Y. Zhishui;Y. HuaL. Qinghua, *Gap bridging of 6061 aluminum alloy joints welded by variable-polarity cold metal transfer.* Journal of Materials Processing Technology, 2018. **255**: p. 927-935.

48. Lin, M.L.T.W. Eagar, *Influence of Arc Pressure on Weld Pool Geometry.* Welding Journal, 1985. **64**(6): p. 163-169.

49. Rokhlin, S.A.C. Guu, *A study of Arc Force, Pool Depression, and Weld Penetration During Gas Tungsten Arc Welding.* Welding Journal, 1993. **72**(8): p. 381-390.

50. Fairchild, D.P.;N.V. Bangaru;J.Y. Koo;P.L. HarrisonA. Ozekcin, *A study concerning intercritical HAZ microstructure and toughness in HSLA steels.* Welding Journal, 1991. **471**(12): p. 321-329.

51. Bunaziv, I.;O.M. Akselsen;J. FrostevargA.F.H. Kaplan, *Laser-arc hybrid welding of thick HSLA steel.* Journal of Materials Processing Technology, 2018. **259**: p. 75-87.

52. Ricks, R.A.;P.R. HowellG.S. Barritte, *The nature of acicular ferrite in HSLA steel weld metals.* Journal of Materials Science, 1982. **17**(3): p. 732-740.

53. Kluken, A.O.Ø. Grong, *Mechanisms of inclusion formation in Al−Ti−Si−Mn deoxidized steel weld metals.* Metallurgical Transactions A, 1989. **20**(8): p. 1335-1349.

54. Shim, J.H.;Y.J. Oh;J.Y. Suh;Y.W. Cho;J.D. Shim;J.S. ByunD.N. Lee, *Ferrite nucleation potency of non-metallic inclusions in medium carbon steels.* Acta Materialia, 2001. **49**(12): p. 2115-2122.

55. Zhang, D.;H. TerasakiY.-i. Komizo, *In situ observation of the formation of intragranular acicular ferrite at non-metallic inclusions in C–Mn steel.* Acta Materialia, 2010. **58**(4): p. 1369-1378.

56. van der Eijk, C.;O. GrongJ. Walmsley, *Mechanisms of inclusion formation in low alloy steels deoxidised with titanium.* Materials Science and Technology, 2000. **16**(1): p. 55-64.

57. Sarma, D.S.;A.V. Karasev; P.G. Jönsson, *On the Role of Non-metallic Inclusions in the Nucleation of Acicular Ferrite in Steels.* ISIJ International, 2009. **49**(7): p. 1063-1074.

58. Babu, S.S.H.K.D.H. Bhadeshia, *Transition from bainite to acicular ferrite in reheated Fe–Cr–C weld deposits.* Materials Science and Technology, 1990. **6**(10): p. 1005–1020.